A MICROMECHANICAL STUDY OF RESIDUAL STRESSES IN FUNCTIONALLY GRADED MATERIALS

MING DAO, PEI GU, AKHILESH MAEWAL and R. J. ASARO

Department of Applied Mechanics and Engineering Sciences, 0411, University of California, San Diego, La Jolla, CA 92093, U.S.A.

Abstract—A physically based computational micromechanics model is developed to study *random* and *discrete* microstructures in functionally graded materials (FGMs). The influences of discrete microstructure on residual stress distributions at grain size level are examined with respect to material gradient and FGM volume percentage (within a ceramic–FGM–metal three-layer structure). Both thermoelastic and thermoplastic deformation are considered, and the plastic behavior of metal grains is modeled at the single crystal level using crystal plasticity theory. The results are compared with those obtained using a continuous model which does not consider the microstructural randomness and discreteness. In an *averaged* sense both the micromechanics model and the continuous model give practically the same macroscopic stresses; whereas the discrete micromechanics model predicts fairly high residual stress concentrations at the grain size level (i.e. higher than 700 MPa in 5–6 vol% FGM grains) with only a 300°C temperature drop in a Ni–Al_2O_3 FGM system. Statistical analysis shows that the residual stress concentrations are insensitive to material gradient and FGM volume percentage. The need to consider microstructural details in FGM microstructures is evident. The results obtained provide some insights for improving the reliability of FGMs against fracture and delamination. © *1997 Acta Metallurgica Inc.*

1. INTRODUCTION

Functionally graded materials (FGMs) are spatial composites within which the composition of each of the two material phases that form the FGMs varies along their thickness direction. The variation is designed to be tailorable so as to achieve predetermined responses to given mechanical and thermal–mechanical loadings. Within a FGM, the different material phases have different functions. In a metal–ceramic FGM, the metal-rich side is placed in the region where mechanical performance, such as toughness, needs to be stronger; and the ceramic-rich side, which has better thermal resistance, is exposed to high temperatures, or placed in the region where there is a potentially severe temperature variation. Also, FGMs can reduce the thermal mismatch at the interfaces of bimaterials and, therefore, largely reduce the possibility of fracture caused by the mismatch. Applications of FGMs include aerospace, power generation, furnaces and others where strong material performance, especially the ability to resist thermal shock, is required or expected.

Material gradients, induced by the change in material properties, make FGMs different in behavior from homogeneous materials and traditional composite materials. Over the past few years, there have been a number of works, both theoretical and experimental, to study the responses of FGMs to mechanical and thermal loads under various loading conditions, for various geometries and in various

deformation and fracture mechanisms, including elastic and plastic aspects and crack propagation [1–11]. Most of the previous studies above focused on the continuous approach which considers that the material properties change continuously, as shown in Fig. 1(b). The continuous model gives correct solutions to such problems as elastic deformation in the ceramic-rich side and plastic deformation in the metal-rich side, when the scale considered is much larger than that of the grain sizes of the constituent material phases. It also gives a good prediction for damage initiation from an imperfection, such as a void or crack, when the size of the imperfection is much larger than the grain size.

The microstructures in FGMs are *discrete* and *random* in nature, as schematically shown in Fig. 1(a). The strongly heterogeneous microstructure is likely, at least possible, to cause locally concentrated residual stresses during thermal or mechanical loading. These locally concentrated stresses, especially those high in tension, may act to initiate small cracks and voids. The development of these small-scale failures may lead to large-scale failures and result in the fracture of the whole structure. Experiments on Si–C FGM by Sohda *et al.* [11] showed that the porous microstructure has a much better resistance against delamination and crack propagation than the companion dense microstructure, where the latter has a higher level of local stresses. Also pointed out by Finot *et al.* [6], to study

the local stress distributions and concentrations within the FGM, microstructural details such as the heterogeneous microstructure and local plastic deformation must be considered carefully. The objective of this study is, therefore, to explore the microstructural *randomness* and *discreteness* vs macroscopic material gradients and geometries with respect to the thermal residual stresses and local residual stress concentrations within FGM microstructures. A discrete computational micromechanics model is developed. In our discrete micromechanics model, the ceramic grains are treated to be elastically deformed as the typical ceramic materials; the metal grains undergo thermo-elastoplastic, finite deformation, and are treated using crystal plasticity theory. The results, as will be seen in the later sections, show that local stress concentration at the grain size level is significant. For the purpose of comparison, we also solve the problem by the continuous model.

The plan of the paper is as follows. Both the continuous and discrete models are described in Section 2, where a brief description is given of the crystal plasticity theory used for metal grains. Numerical results are presented in Section 3. In Section 3.1, results using the continuous model are presented, where influences of different gradients on macroscopic residual stresses are reviewed. In Section 3.2, results using the discrete micromechanics model are presented, the macroscopic residual stresses as well as the local stress concentrations are explored using different material gradients and FGM volume

percentages. In Section 3.3, the contribution of plastic deformation within the discrete micromechanics model is studied. In Section 3.4, a short summary is given on the statistical analysis of the residual stress concentrations with respect to material gradient, FGM volume percentage as well as the plastic relaxation. Finally, discussions and conclusions follow in Section 4.

2. THE CONTINUOUS AND DISCRETE MODELS

The model geometry, as shown in Fig. 2, consists of three layers: the ceramic layer is on the left side; the metal layer is on the right side; and the FGM is sandwiched between them. As a model system, we choose the metal to be Ni, and the ceramic to be Al_2O_3 in this study. The FGM is, therefore, Ni–Al_2O_3 FGM. Both continuous and discrete models for the FGM, including the numerical consideration, are described below.

2.1. The continuous model

We define x as the relative distance from the ceramic–FGM interface, i.e. $x = 0$ stands for the ceramic–FGM interface and $x = 1$ stands for the FGM–metal interface. For the continuous model for the FGM, the effective material properties are assumed to follow the "rule of mixture":

$$A(x) = V_{Metal}(x)A_{Metal} + V_{Ceramic}(x)A_{Ceramic}, \quad (1)$$

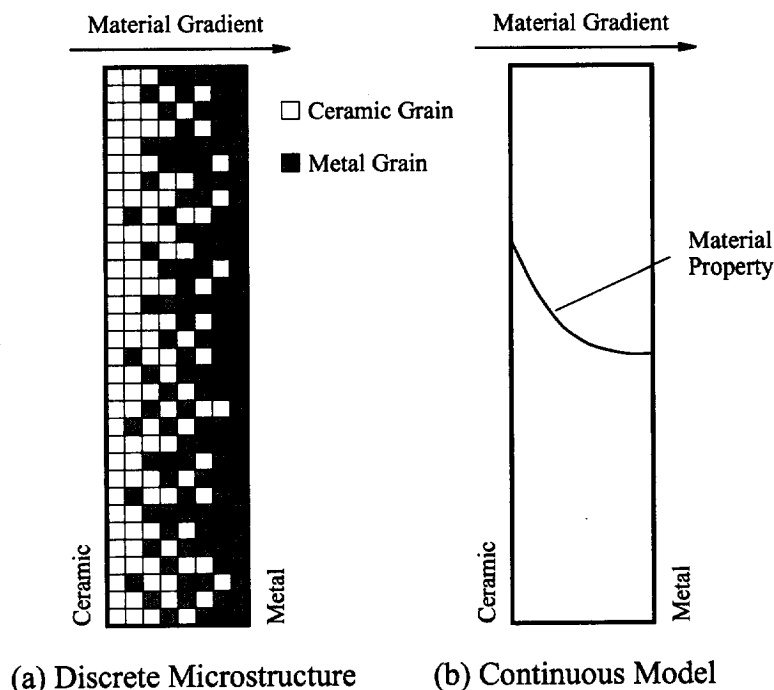(a) Discrete Microstructure   (b) Continuous Model

Fig. 1. Schematic drawings of functionally graded materials (FGMs): (a) discrete and random microstructure in reality, and (b) continuous gradient modeling often used.
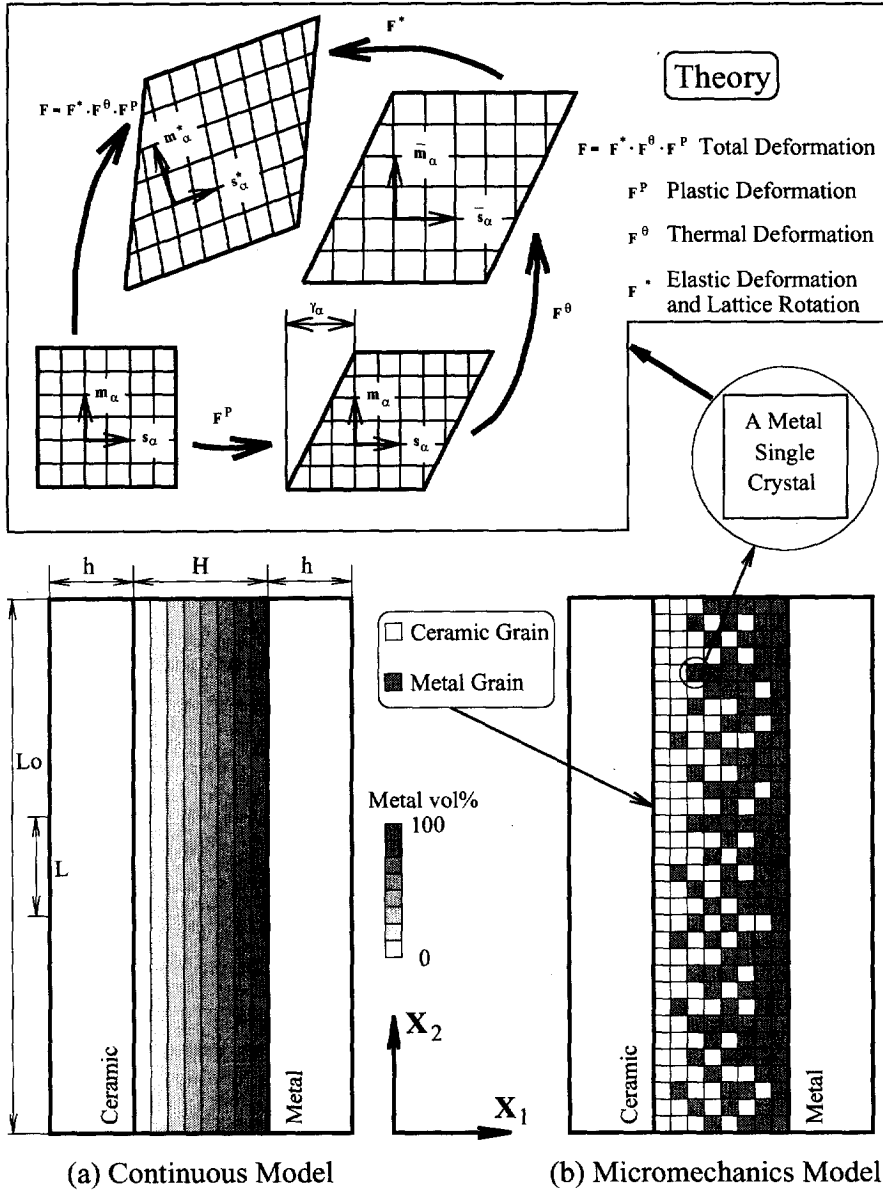
Fig. 2. Schematic drawings of ceramic–FGM–metal three-layer structures used to model the functionally graded materials, with (a) continuous model and (b) discrete micromechanics model. The insert to (b) shows the deformation gradient decomposition for a metal single crystal.

where A stands for either the elastic constants, E (Young's modulus) and v (Poisson's ratio), or the thermal expansion coefficient α; $V_{\text{Metal}}(x)$ and $V_{\text{Ceramic}}(x)$ are the volume fractions of metal and ceramic, respectively, at the position x. The simplified material property form overlooks the interactions of the two material phases at the microscopic level, so it leads to an approximate solution. The more accurate material property variation form at the macroscopic level requires a better understanding of FGM microstructure and its deformation, which are the focus of this study. We will only obtain the elastic solution for the continuous model, and it is mainly for comparison with the solution obtained by the

discrete model. Plastic deformation of the sandwich structure was studied using a continuous model in Giannakopoulos *et al.* [5] and Finot *et al.* [6].

The thermoelastic solution in this case may be obtained analytically [5]. Here, a finite element method is used for the purpose of examining its accuracy for FGMs. In the implementation, the FGM layer is divided into 30 micro-layers, as shown schematically in Fig. 2(a), and the material properties of each micro-layer are taken to be constants.

2.2. The discrete micromechanics model

We have developed a computational micromechanics model for FGMs using the crystal plasticity

theory. Figure 2(b) shows the model geometry for a FGM consisting of the metallic and ceramic grains randomly distributed within it. The macroscopic material properties obtained by statistical processing of the random distribution of the metal and ceramic grains vary continuously along the thickness direction, and give their desired variation forms. Each of the metal grains has its own crystal orientation (also randomly distributed) which is shown by the angle ψ in Fig. 3, and its thermoplastic behavior is assumed to be governed by crystal plasticity theory. The ceramic grains are modeled using the standard linear elasticity theory.

The two-dimensional idealization shown in Fig. 3 was introduced by Harren *et al.* [12], Harren and Asaro [13] and McHugh *et al.* [14] for f.c.c. or b.c.c. polycrystals and their metal matrix composites. The three slip systems are arranged in an equilateral triangle, and the reference laboratory base vectors $\mathbf{X}_i$ are at an angle ψ with respect to reference crystal base vectors $\mathbf{a}_i$. The slip directions in this model geometry, $\mathbf{s}_1$, $\mathbf{s}_2$ and $\mathbf{s}_3$, represent the close-packed directions of an assemblage of close-packed circular cylinders. Since, in a two-dimensional model two independent slip systems can accommodate arbitrary increment of plastic strain, the three independent slip systems here resemble the redundancy exhibited by both f.c.c. and b.c.c. crystals. We note that using traditional metal plasticity theories (i.e. J_2 flow theory) would give us similar results for Ni (f.c.c.). If any low-symmetry crystals (say NiAl or TiAl) are involved, then crystal plasticity theory is necessary to account for the orientation dependent deformation behavior.

The single crystal constitutive theory, in its present form, was developed by Asaro and his coworkers [14–21]. The theory which will be briefly described below builds on the pioneering work by Taylor [22] and Hill and Rice [23].

The total deformation gradient is decomposed into plastic ($\mathbf{F}^{\mathrm{P}}$), thermal ($\mathbf{F}^{\theta}$), and lattice ($\mathbf{F}^{*}$) parts, as shown in the insert of Fig. 2(b). If $\mathbf{u}$ is the displacement vector and $\mathbf{X}$ the material position vector with respect to the reference (undeformed) state, $\mathbf{F} = \mathbf{I} + \partial\mathbf{u}/\partial\mathbf{X}$ ($\mathbf{I}$ is the second-order identity tensor) and

$$\mathbf{F} = \mathbf{F}^{*}\cdot\mathbf{F}^{\theta}\cdot\mathbf{F}^{\mathrm{P}}. \tag{2}$$

Plastic deformation occurs by the flow of material through the lattice, via simple shearing, across planes with unit normals $\mathbf{m}_{\alpha}$ and in directions $\mathbf{s}_{\alpha}$; here $\mathbf{m}_{\alpha}$ and $\mathbf{s}_{\alpha}$ represent a crystallographic slip plane normal and a slip direction, respectively, and α is an index that designates a slip system. If $\dot{\gamma}_{\alpha}$ is the slip rate on the α slip system, then the velocity gradients of this plastic shear flow can be written as

$$\dot{\mathbf{F}}^{\mathrm{P}}\cdot\mathbf{F}^{\mathrm{P}-1} = \sum_{\alpha}\dot{\gamma}_{\alpha}\mathbf{s}_{\alpha}\mathbf{m}_{\alpha}, \tag{3}$$

where the summation is over all active slip systems. The thermal parts of the velocity gradients are described as

$$\dot{\mathbf{F}}^{\theta}\cdot\mathbf{F}^{\theta-1} = \dot{\theta}\boldsymbol{\alpha}; \quad \boldsymbol{\alpha} = \sum_i\sum_j\alpha_{ij}\mathbf{a}_i\mathbf{a}_j, \tag{4}$$

where θ represents temperature and $\boldsymbol{\alpha}$ is a tensor whose components, α_{ij}, with respect to the time independent Cartesian base vectors, $\mathbf{a}_i$, are the thermal expansion coefficients. The base vectors are aligned with the crystal lattice in the reference configuration in some standard way, e.g. in cubic crystals. It is most convenient to align the $\mathbf{a}_i$ base vectors with the cube axes, in which case $\boldsymbol{\alpha}$ would be diagonal with all components equal.

In general, $\dot{\gamma}_{\alpha}$ will be a function of temperature, stress state and material state. As a specific example we have used expressions such as

$$\dot{\gamma}_{\alpha} = \dot{a}\,\mathrm{sgn}\{\tau_{\alpha}\}\left\{\left|\frac{\tau_{\alpha}}{g_{\alpha}}\right|\right\}^{1/n} \tag{5}$$

to represent strain rate sensitive power-law type behavior. In the expression, n is the material rate sensitivity parameter, τ_{α} is the resolved shear stress on the slip system α, and $g_{\alpha} > 0$ is its current strength.

The slip system hardness, g_{α}, is obtained by the path-dependent integration of the evolution equations of the form:

$$\dot{g}_{\alpha} = \sum_{\beta}h_{\alpha\beta}(\gamma_{\mathrm{a}})|\dot{\gamma}_{\beta}| + g_{\alpha}^{\theta}\dot{\theta}; \quad \gamma_{\mathrm{a}} = \int_0^t\sum_{\alpha}|\dot{\gamma}_{\alpha}|\,\mathrm{d}t, \tag{6}$$

where γ_{a} is the accumulated sum of slips, $h_{\alpha\beta}$ is a matrix of hardening moduli and g_{α}^{θ} is the rate of change of slip system hardness with respect to temperature alone. The initial condition for this
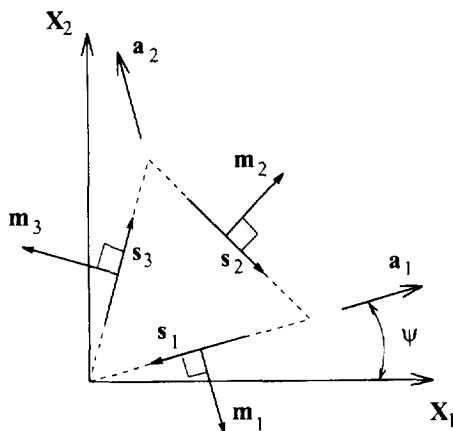

Fig. 3. Two-dimensional model single crystal slip geometry used for metal grains. The three slip systems are arranged in an equilateral triangle, and the reference laboratory base vectors $\mathbf{X}_i$ are at an angle ψ with respect to reference crystal base vectors $\mathbf{a}_i$.

Table 1. Elastic properties used for the computations

	E (GPa)	ν	α (K^{-1})
Al$_2$O$_3$	380	0.25	7.4×10^{-6}
Ni	214	0.35	15.4×10^{-6}

evolution is given by

$$g_\alpha(\gamma_a = 0, \theta) = g_0(\theta), \qquad (7)$$

where θ is the temperature.

The detailed development of these constitutive relations can be found in McHugh et al. [14]. This constitutive theory has been implemented into finite element codes, using a rate tangent method introduced by Pierce et al. [18].

3. RESULTS

The geometry of the sandwich structure is specified in Fig. 2. To avoid the edge effects, the total length/width ratio ($L_0/(H + 2h)$) was chosen to be 5, while only the center part with length $L(L < 0.25L_0)$ was considered when performing residual stress analysis. Two sets of FGM interlayer thickness, i.e. $H/(H + 2h) = 40$ and 70 vol%, were used.

To make this complicated boundary value problem manageable computationally, a relatively coarse mesh (i.e. four triangular elements per grain) is used in this study and simple square grains are employed. Doing so, as Taylor [22, 24] and many others [25–27] did successfully in modeling polycrystalline materials, effectively treats the deformation within each individual grain as uniform. The finite element model, however, takes the interactions between all constituent grains into consideration, which is not achievable using Taylor or Sachs type models. In studying the interactions at the grain size level, this model design is at least a first-order approximation. Also, in keeping all the microstructural "building blocks" (i.e. ceramic and metal grains in the discrete model) exactly the same, the relative importance of material gradient and FGM volume percentage can be identified.

The specific FGM system is the Al$_2$O$_3$–Ni system. In this study, the major focus is on the relative importance of the discrete and random microstructure vs FGM volume fraction and gradient functional form. With that in mind, and noting that all the case studies shown later were performed under a relatively small (300°C) temperature variation, for simplicity the elastic properties were taken to be constants. The material properties used for the computations are listed in Tables 1 and 2. A two-dimensional plane
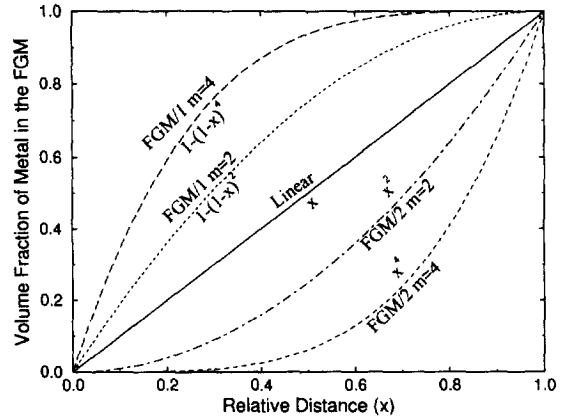

Fig. 4. Different gradient functions used in the residual stress analysis.

strain deformation condition was imposed. The thermal loading was induced by cooling the structure by 300°C. The temperature was assumed to be uniform within the three-layer structure, and the sandwich structure was set to be stress free at the beginning temperature. For the metal grains, linear interpolation was used to obtain the temperature-dependent critical resolved shear stresses $g_0(\theta)$ in equation (7) between the several temperatures shown in Table 2. The shear strain hardening h in equation (6) was taken to be 77.4 MPa, which was converted from the data in Ref. [28] using a Taylor factor of 3.06 for f.c.c. polycrystals with the linear hardening assumption. A low material rate sensitivity parameter is given as $n = 0.005$ in equation (5).

We write V_{FGM} as the volume fraction of Ni within the FGM layer, and x as the relative distance from the Al$_2$O$_3$–FGM interface (i.e. $x = 0$ stands for the Al$_2$O$_3$–FGM interface and $x = 1$ stands for the FGM–Ni interface). As shown in Fig. 4, three functional forms were used in the computations:

$$\text{Linear:} \quad V_{FGM}(x) = x, \qquad (8a)$$

$$\text{FGM}/1: \quad V_{FGM}(x) = 1 - (1 - x)^m, \quad m = 2, 4, \quad (8b)$$

$$\text{FGM}/2: \quad V_{FGM}(x) = x^m, \quad m = 2, 4. \quad (8c)$$

When $m = 1$, both FGM/1 and FGM/2 reduce to the linear case of equation (8a), and when $m \geqslant 2$ functions in the FGM/1 class have zero slope at the FGM–Ni interface ($x = 1$), whereas the functions in the class FGM/2 have zero slope at the Al$_2$O$_3$–FGM interface ($x = 0$).

Table 2. Plastic properties of Ni grains used in the computations

T (°C)	20	127	227	327	427	527	627	727	827
σ_y^a (MPa)	148	153	140	138	115	100	69	59	45
τ_{CRSS}^b (MPa)	48.4	50.0	45.8	45.1	37.6	32.7	22.5	19.3	14.7

[a] Data from Suresh et al. [28].
[b] Calculated from σ_y with a Taylor factor of 3.06.

3.1. The continuous model—macroscopic stresses vs material gradients and FGM volume percentages

For this problem, the only non-zero stress component is the in-plane normal stress along the X_2 direction. Figures 5(a) and (b) show the results of the in-plane normal stress distribution along the X_1 direction for the 40 and 70 vol% FGM, respectively. Due to the presence of the FGM layer, the stresses are continuous, and have continuous derivatives wherever the material property variation function in equations (8) is. It is noteworthy that although the existence of the FGM layer in general decreases the stress at one or both of the interfaces, for power index $m \leqslant 2$ in equations (8), there is an extremum in the FGM layer, and this extremum in some cases has a magnitude close to that of the normal stress at the interface in the base-line case, i.e. a sharp ceramic–metal interface without the FGM layer [29]. Comparing Fig. 5(b) with Fig. 5(a), it is found that, in general, increasing the relative FGM volume percentage decreases the stress at one or both of the interfaces. These results are similar to those found in Giannakopoulos et al. [5].

Next, we will explore how the local stress concentrations interact with material gradient as well as the FGM volume percentage. The averaged physical meaning of the continuous solution will be clearer when we present the discrete solution below and compare the two solutions.

3.2. The discrete model—local stress concentrations and macroscopic stresses

In this section, the discrete micromechanics model is used and only elastic deformation is considered. Plasticity effects will be studied in the next section.

Figure 6 shows contour plots of (a) σ_{22}, and (b) averaged in-plane principal stress ($p = (\sigma_{11} + \sigma_{22})/2$) developed in the 40 vol% FGM with linear gradient. It is clearly seen that the local stress concentration is quite high and the stress field is very inhomogeneous, i.e. the stress variations among many of the adjacent grains are significant. The σ_{11} was also found to be

inhomogeneous. Due to the thermal mismatch between ceramic grains and metal grains, most metal grains experience large tensile stresses; and this is especially true for metal grains near the ceramic–FGM interface and those in the middle region of the FGM layer.

Additional computations were performed using different gradient functions. Figure 7 shows contour plots of averaged in-lane principal stress ($p = (\sigma_{11} + \sigma_{22})/2$) developed in the 40 vol% FGM with (a) gradient function $V_{FGM} = 1 - (1 - x)^2$ (FGM/1 $m = 2$), and (b) gradient function $V_{FGM} = x^2$ (FGM/2 $m = 2$). The distribution of stresses is quite different with different gradient functions, as can be seen clearly from Figs 6(b), 7(a) and 7(b). Detailed examination of Figs 6 and 7 tells us that, in almost every local region (say take 5×5 grains as the region size) where the ceramic grains are more than 40 vol%, there are always some metal grains experiencing significant tensile stresses for all three cases. The results for the 70 vol% FGM were similar to those for the 40 vol% FGM.

For such discrete and random microstructures, more physical insights can be gained via the statistical analyses of the stress distribution. Figure 8(a) shows the distribution profiles of $p = (\sigma_{11} + \sigma_{22})/2$ developed in the FGM layer (40 vol% FGM) with three different gradient functions; Fig. 8(b) shows the distribution profiles of p developed in the FGM layer (linear gradient) of a 40 and a 70 vol% FGM, respectively. The three distribution profiles in Fig. 8(a) are distinctively different: (i) the distribution peak between 50 and 200 MPa (mostly in metal grains) drops as the total metal composition in the FGM layer decreases; and (ii) the distribution peak between -50 and -250 MPa (mostly developed in ceramic grains) increases as the total ceramic composition in the FGM layer increases. The FGM volume percentage also has large influences on the distribution profile of p, see Fig. 8(b): the distribution peak for tensile stresses shifted from around 110 MPa (40 vol% FGM) to about 50 MPa (70 vol% FGM); and the distribution peak for compressive stresses
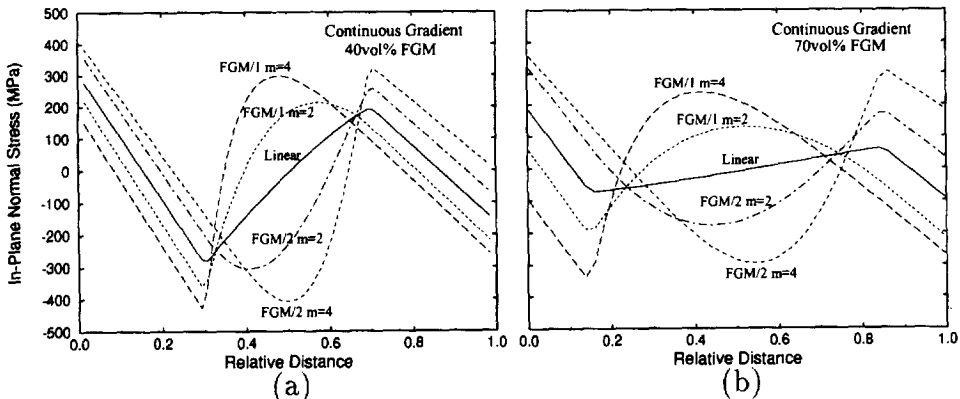

Fig. 5. In-plane normal stress distributions along the X_1 direction using the continuous model with (a) 40 and (b) 70 vol% FGM, respectively.
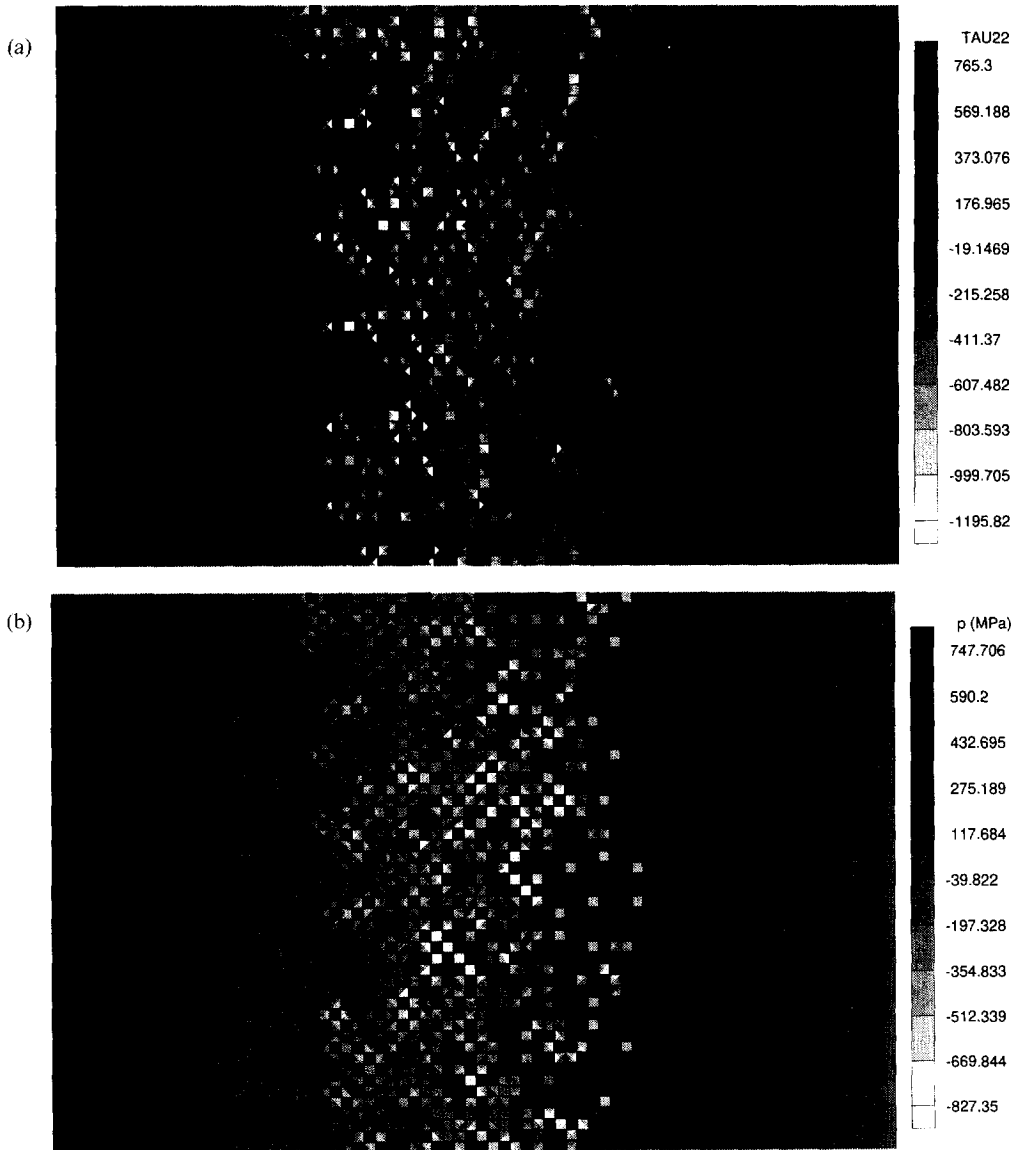
Fig. 6. Contour plots of (a) σ_{22}, and (b) averaged in-plane principal stress ($p = (\sigma_{11} + \sigma_{22})/2$) developed within the linear gradient, 40 vol% FGM. Only elastic deformation is considered here.

shifted from around -150 MPa (40 vol% FGM) to about -50 MPa (70 vol% FGM). However, the distribution profile for high stresses, i.e. for $p \leqslant 500$ MPa or $p \geqslant -500$ MPa, are found to be insensitive to material gradient and FGM volume percentage.

Finally, for the purpose of comparison, we averaged the stresses over each column of elements to get the mean stress along the vertical direction. Figure 9 shows the macroscopically averaged in-plane normal stress developed within the discrete microstructures (shown by separated symbols) as compared to the curves obtained using the continuous model (shown by continuous lines). It is interesting to see that, although there are a lot of local stress concentrations, the two types of modeling

approach given practically the same averaged (or macroscopic) stresses. In an averaged sense, only small variations can be found in Fig. 9 for the discrete microstructure model due to the local randomness and discreteness. This shows that the macroscopic stresses are those based on a scale much larger than the grain size and obtained without considering certain details, such as local stress concentrations, at a smaller scale.

3.3. The discrete model—influence of plastic deformation

In this section, we explore the effects of plastic deformation within the metal grains in the discrete microstructure. Besides the concentrated stresses, large, locally concentrated plastic strain accum

lation during repeated thermal cycling may also initiate failure.

Figure 10 shows the contour plots of (a) averaged in-plane principal stress ($p = (\sigma_{11} + \sigma_{22})/2$), and (b) accumulated sum of slips (γ_a) developed in the linear gradient, 40 vol% FGM. The temperature drop was from 700 to 400°C, and the plasticity parameters were taken to be as listed in Table 2. Similar to the thermoelastic case, the stress distribution is again inhomogeneous, with many metal grains experiencing high tensile stresses and many ceramic grains experiencing high compressive stresses. If we compare Fig. 10(a) with Fig. 6(b) (elasticity only), the stress concentration in the ceramic grains is significantly reduced in the region where metal content is greater than 70 vol%, due to plastic relaxation. With only a

300°C temperature drop, Fig. 10(b) shows that: (i) there are plastic strain accumulations in many of the metal grains, and (ii) certain sites have relatively high strain accumulations, about 1.5%. The high strain accumulation sites seem to appear in the regions where metal content is between 50 and 75 vol%.

Figure 11 shows the distribution profiles of p ($= (\sigma_{11} + \sigma_{22})/2$) developed within the FGM layer (linear gradient, 40 vol% FGM), for both the elastic and the elastoplastic case. The plastic relaxation effect is very clear here in this case, where stresses are in general shifting to lower magnitudes with plasticity. The distribution profile for high tensile stresses with $p \geqslant 700$ MPa, however, has reduced only slightly with plastic relaxation. Similar to the thermoelastic case, the stress distribution profile for
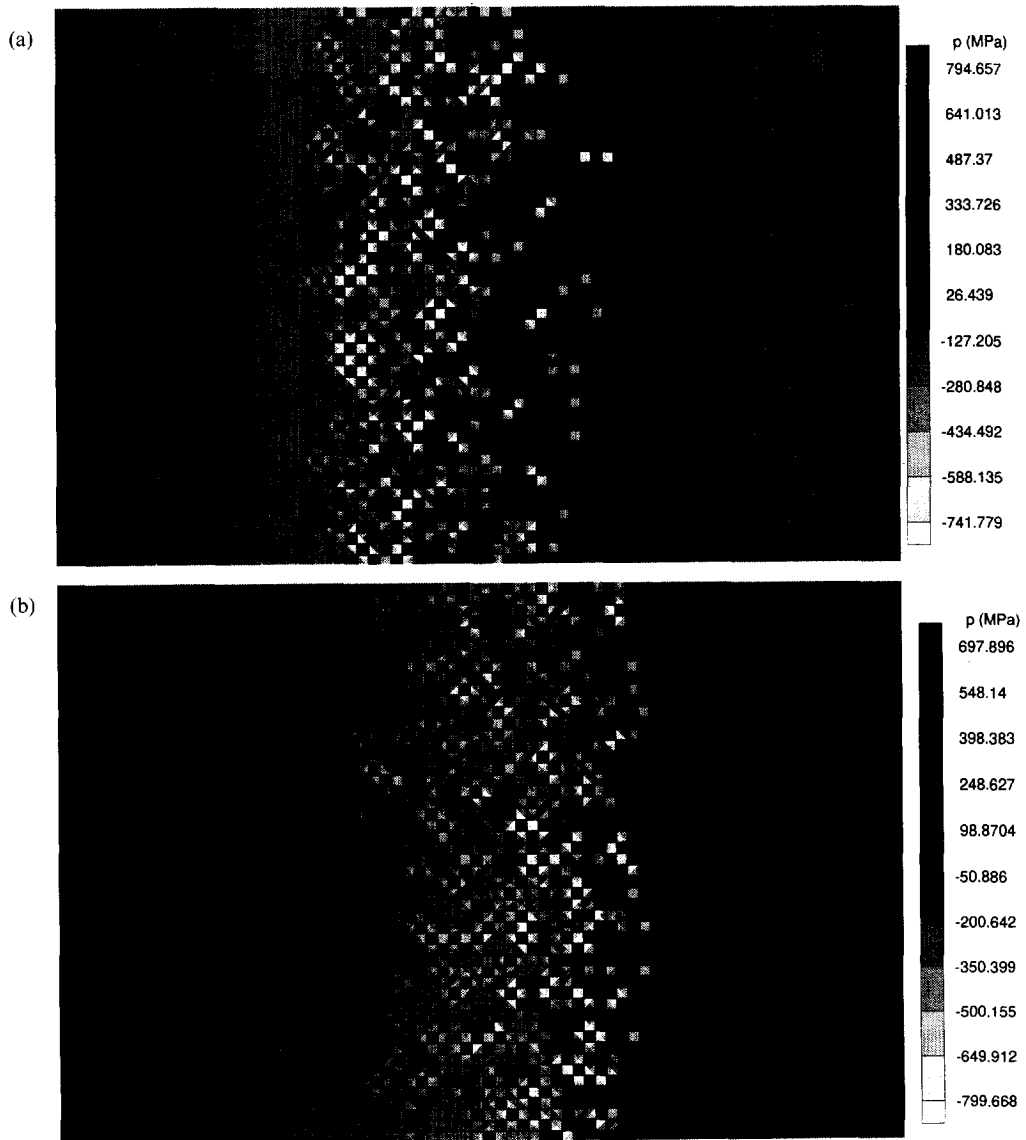

Fig. 7. Contour plots of averaged in-plane principal stress ($p = (\sigma_{11} + \sigma_{22})/2$) developed in the 40 vol% FGM with (a) gradient function $V_{FGM} = 1 - (1 - x)^2$ (FGM/1 $m = 2$), and (b) gradient function $V_{FGM} = x^2$ (FGM/2 $m = 2$). Only elastic deformation is considered here.
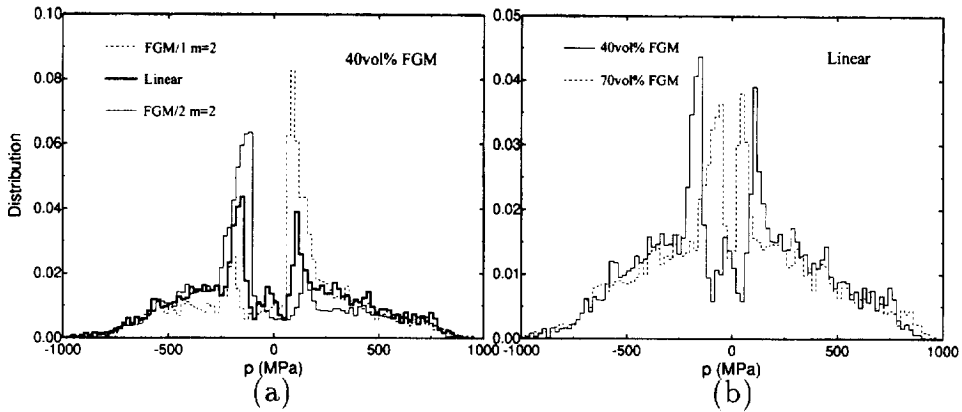
Fig. 8. (a) Averaged in-plane principal stress ($p = (\sigma_{11} + \sigma_{22})/2$) distribution profiles developed within the FGM layer (40 vol% FGM) with three different gradient functions; and (b) distribution profiles of p developed in the FGM layer (linear gradient) of a 40 and a 70 vol% FGM, respectively.

high tensile stress regions is insensitive to material gradient and FGM volume percentage. On the other hand, the distribution profile for high compressive stresses with $p \leqslant -250$ MPa (mostly in ceramic grains) drops significantly. This suggest that, when ceramic grains are subject to tensile stresses *if temperature increases*, the plastic relaxation effects may reduce their tensile stress concentrations.

We average the stresses over each column of elements for the plastic solution to obtain the averaged in-plane normal stress. Figure 12 plots the macroscopically averaged stress for both the elastic and the elastoplastic case. Comparing Fig. 12 with Fig. 10(b), it is found that the metal rich section and part of the pure metal region are under general macroscopic yielding, which sets the maximum magnitude of the macroscopic stresses for the plastic case.

3.4. The statistical analysis of residual stress concentrations—averaged peak stress

Since the stress distribution profiles of p for the high stress area shown in Figs 8 and 11 are small, to
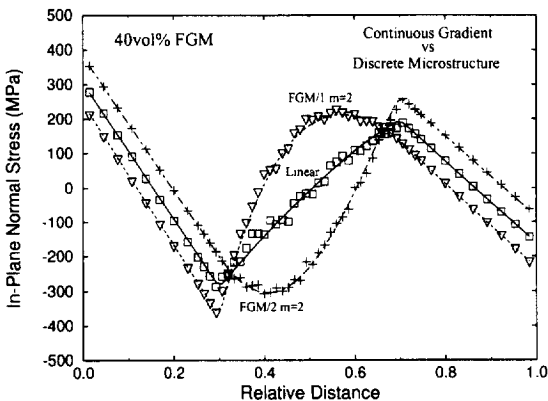

Fig. 9. Macroscopically averaged in-plane normal stress developed within the discrete microstructures (shown by separated symbols) as compared to the curves obtained using the continuous model (shown by continuous lines).

get more reliable statistical results we employ 6 vol% APSP to treat the data in these figures. The 6 vol% APSP (averaged peak stress of p) is the stress p averaged over the 6 vol% microstructure of the FGM layer which has the highest tensile stresses (p). Similarly, we can obtain 3 vol% APSP, 9 vol% APSP etc. Figure 13 shows the 6 vol% APSP (averaged peak stress of p) for different material gradients and different FGM volume percentages, and for both the elastic solution (marked with El) and the elastoplastic solution (marked with Pl). From Fig. 13, the distribution profile for high tensile stresses is again found to be insensitive to material gradient and FGM volume percentage, and the plastic relaxation effect is relatively small for the high stress regime. Similar conclusions can be drawn from the 3 vol% APSP (averaged peak stress of p).

The above statistical results are interpreted by the following observations. As mentioned before, high tensile stresses always occur in those metal grains surrounded by many ceramic grains. Comparing those stresses in Figs 5 and 9, the stress concentrations in these metal grains are found to be an order of magnitude higher than the macroscopic stresses in the FGM layer. Considering the large number of stiff ceramics around each of those metal grains, the high local stresses are believed to be insensitive to the macroscopic physical parameters. The effect of material gradient and FGM percentage on the macroscopic stresses is mainly due to the change of the distribution profiles in the middle parts of Figs 8 and 11, which have lower magnitude of stresses.

For the small plastic relaxation for local stress concentrations shown in Fig. 13, this can also be related to the fact that peak tensile stresses always occur in metal grains where a lot of ceramic grains are surrounded. The general stress state induced in such metal grains is mostly all around tension, i.e. $\sigma_1 \approx \sigma_2$ where σ_1 and σ_2 are the two in-plane principal stresses. With $\sigma_1 \approx \sigma_2$, the maximum shear stress $\tau_{max} = (\sigma_1 - \sigma_2)/2$ is therefore small. No matter how

(a)

(b)
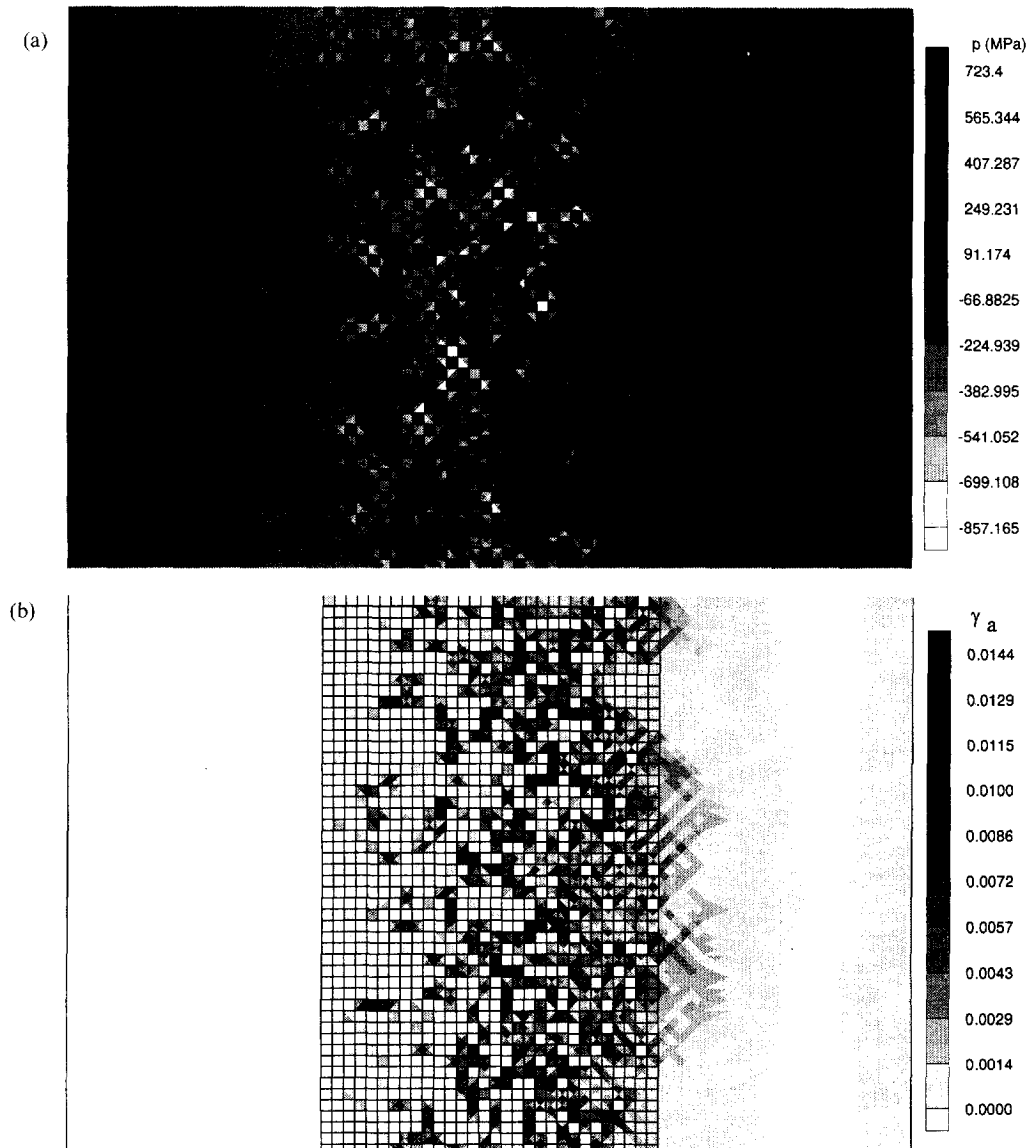
Fig. 10. Contour plots of (a) averaged in-plane principal stress ($p = (\sigma_{11} + \sigma_{22})/2$), and (b) accumulated sum of slips (γ_a) developed in the linear gradient, 40 vol% FGM. Plastic deformation is considered here.

low the yield strength is in the metal grains, small shear stresses can hardly produce any plastic deformation, and therefore are not helpful in relaxing this kind of stress state.

4. DISCUSSION

A physically based micromechanical model is developed to study residual stress distributions and concentrations in the FGM sandwiched between two dissimilar materials during thermal loadings. The results obtained reveal detailed information of microstructural behavior at the grain size level, and thus provide some insights for optimizing FGMs and the control of their failures.

It is stressed that the scale level we are concerned with in this study is at the grain size level and

upwards. Using the relatively coarse mesh and square "building blocks" is a first-order approximation to the reality, and not intended for subgrain level microscopic features. For example, a very refined mesh will show very high stress concentrations (in fact singularities) at the inter-phase corners. Due to the relative small $E_{Al_2O_3}/E_{Ni}$ ratio (1.77), the singularity is a fairly weak one, which means high stress regions will only occupy a very small volume fraction. It is shown that in the case of two elastic bonded quarter planes, the order of the singularity is about 0.05 ($1/r^\alpha$, $\alpha = 0.05$) for such an elastic difference, see Bogy [30]. This kind of singularity is thus expected to have little (i.e. second order) effect on the averaged grain level stress. However, if 5–6 vol% of the FGM grains have some averaged tensile stresses higher than
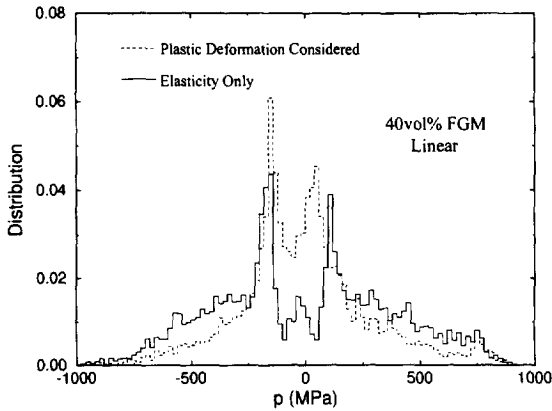
Fig. 11. Averaged in-plane principal stress ($p = (\sigma_{11} + \sigma_{22})/2$), distribution profiles developed within the FGM layer (40 vol% FGM, linear gradient) for both the elastic and the elastoplastic case.
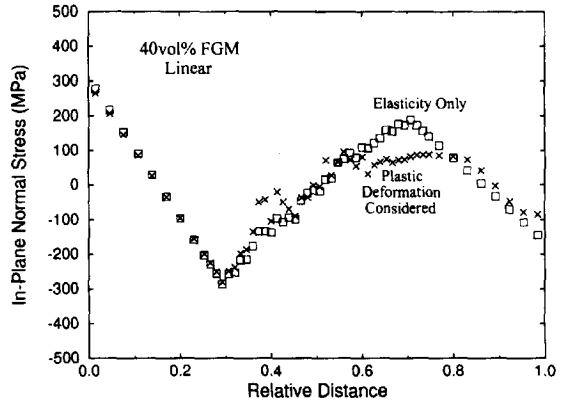

Fig. 12. Macroscopically averaged in-plane normal stress developed within the discrete microstructure (40 vol% FGM, linear gradient), for both the elastic and the elastoplastic case.

700–800 MPa, only higher local stresses can be expected near those subgrain level microscopic features.

The grain level microscopic stress concentrations are found to be quite high, of the order of 800 MPa, with only a 300°C temperature drop; whereas the macroscopic stresses are much lower than the microscopic stresses. This suggests that, if high tensile stress concentration at the grain size level is the failure initiation mode at this size scale, there are always micro-fractures at the grain size scale during thermal loading. Since the stress distribution profile for the high stress region is quite insensitive to material gradient and FGM volume percentage as shown in Section 3, the above conclusion is independent of those two macroscopic parameters. On the other hand, the high stress region in the stress distribution profile is relatively small (about

5–6 vol% with stress p above 700 MPa). Whether the small-scale micro-fractures at the grain size level will develop into large-scale fractures to cause the fatal damage of the whole structure depends on other factors whose effects require further investigation, such as stress redistribution after small-scale failure initiation, loading history and the grain boundary adhesion between the adjacent grains. The present computational micromechanics model can be extended to account for these influences.

For optimizing the microstructure, since the dense structure results in high local stress concentrations, our results suggest that for achieving higher toughness the porous microstructure should be considered; and this is consistent with the experimental observation by Sohda et al. [11] on the Si–C FGM. Their experiments showed that the porous microstructure has a much better resistance against
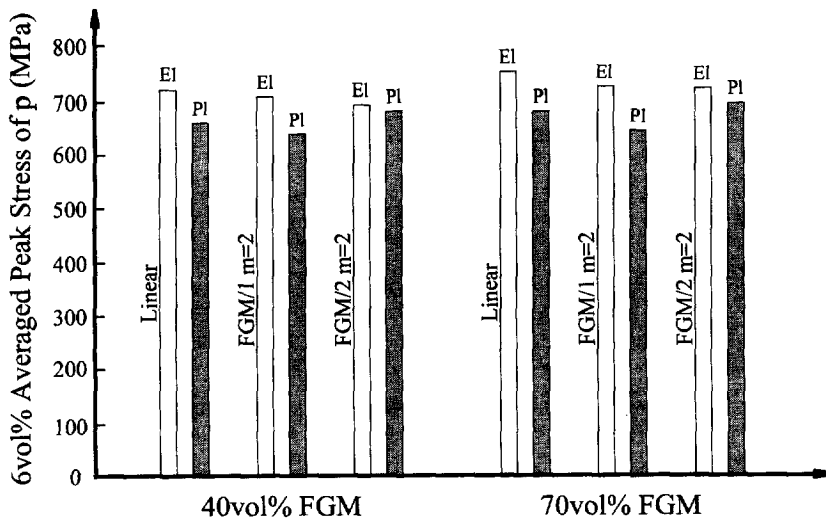

Fig. 13. The 6 vol% averaged peak stress of p (APSP) developed in FGM microstructures with different material gradients and different FGM volume percentages for both the elastic solution (marked with "El" on top) and the elastoplastic solution (marked with "Pl" on top).

cracking than the dense microstructure. Also, in a recent review paper, Koizumi and Niino [31] listed micropore as one of the most important material constituencies in FGM microstructures. Regarding the grain size, the extent of micro-fracturing exhibits large sensitivity to the grain size in ceramic polycrystals subject to thermal loading, being more severe in coarse grained ceramics [32, 33]; therefore, a fine grain sized microstructure is suggested to improve the FGM's resistance against cracking and delamination.

Other microstructural factors, such as grain shape, grain size and third-phase particle, are beyond the scope of the present work, and are the considerations of later studies. The results shown here have clearly demonstrated the need to consider microstructural details in modeling FGMs for determining their mechanical behavior: due to the microstructural discreteness, local residual stress concentrations play a very important role in failure initiation.

REFERENCES

1. Niino, M., Hirai, T. and Watanabe, R., *J. Jpn. Soc. Comp. Mater.*, 1987, **13**, 257.
2. Yamanouchi, M., Koizumi, M., Hirai, T. and Shiota, I. ed., *Proc. 1st Int. Symp. Functionally Gradient Materials*. FGM Forum, Tokyo, Japan, 1990.
3. Holt, J. B., Koizumi, M., Hirai, T. and Munir, Z. A. ed., *Functionally Gradient Materials, Proc. 2nd Int. Symp. Functionally Gradient Materials*, San Francisco, CA, 1992.
4. Pindera, M. J., Arnold, S. M., Aboudi, J. and Hui, D. ed., *Compos. Engng*, 1994, **4**, 1.
5. Giannakopoulos, A. E., Suresh, S., Finot, M. and Olsson, M., *Acta metall.*, 1995, **43**, 1335.
6. Finot, M., Suresh, S., Bull, C. and Sampath, S., *Materi. Sci. Engng A*, 1996, **205**, 59.
7. Aboudi, J., Pindera, M. J. and Arnold, S. M., *Int. J. Solids Struct.*, 1994, **31**, 1393.
8. Aboudi, J., Pindera, M. J. and Arnold, S. M., *Int. J. Solids Struct.*, 1995, **32**, 1675.
9. Noda, N. and Jin, Z., *Int. J. Solids Struct.*, 1993, **30**, 1039.
10. Gu, P. and Asaro, R. J., *Int. J. Solids Struct.*, 1997, **34**, 1.
11. Sohda, Y., Kude, Y., Uemura, S., Saitoh, T., Wakamatsu, Y. and Niino, M., in *Functionally Gradient Materials*, ed. J. B. Holt, M. Koizumi, T. Hirai and Z. A. Munir. San Francisco, CA, November, 1992, p. 125.
12. Harren, S. V., Déve, H. E. and Asaro, R. J., *Acta metall.*, 1988, **36**, 2435.
13. Harren, S. V. and Asaro, R. J. *J. Mech. Phys. Solids*, 1989, **37**, 191.
14. McHugh, P. E., Asaro, R. J. and Shih, C. F., *Acta metall.*, 1993, **41**, 1461.
15. Asaro, R. J. and Rice, J. R., *J. Mech. Phys. Solids*, 1977, **25**, 309.
16. Asaro, R. J., *Acta metall.*, 1979, **27**, 445.
17. Peirce, D., Asaro, R. J. and Needleman, A., *Acta metall.*, 1982, **30**, 1087.
18. Peirce, D., Asaro, R. J. and Needleman, A., *Acta metall.*, 1983, **31**, 1951.
19. Dao, M. and Asaro, R. J., *Mater. Sci. Engng A*, 1993, **170**, 143.
20. Dao, M. and Asaro, R. J., *Mech. Mater.*, 1996, **23**, 71.
21. Dao, M. and Asaro, R. J., *Mech. Mater.*, 1996, **23**, 103.
22. Taylor, G. I., *J. Inst. Metals*, 1938, **62**, 307.
23. Hill, R. and Rice, J. R., *J. Mech. Phys. Solids*, 1972, **20**, 401.
24. Taylor, G. I., in *Stephen Timoshenko 60th Anniversary Volume*, ed. J. M. Lessels. Macmillan, New York, 1938, pp. 218.
25. Asaro, R. J. and Needleman, A., *Acta metall.*, 1985, **33**, 923.
26. Molinari, A., Canova, G. R. and Ahzi, S., *Acta metall.*, 1987, **35**, 2983.
27. Kalidindi, S. R., Bronkhorst, C. A. and Anand, L., *J. Mech. Phys. Solids*, 1992, **40**, 537.
28. Suresh, S., Giannakopoulos, A. E. and Olsson, M., *J. Mech. Phys. Solids*, 1994, **42**, 979.
29. Maewal, A. and Asaro, R. J., Technical Report for ONR Contract No. N00014-94-C-0113, Trans-Science Corporation, 1995.
30. Bogy, D., *J. appl. Mech.*, 1968, **35**, 460.
31. Koizumi, M. and Niino, M., *MRS Bull.*, 1995, **20**(1), 19.
32. Rice, R. W. and Pohanka, R. C., *J. Am. Ceram. Soc.*, 1979, **62**, 559.
33. Ortiz, M. and Molinari, A., *J. Mech. Phys. Solids*, 1988, **36**, 385.